

Fe-Cluster Pushing Electrons to N-Doped Graphitic Layers with Fe₃C(Fe) Hybrid Nanostructure to Enhance O₂ Reduction Catalysis of Zn-Air Batteries

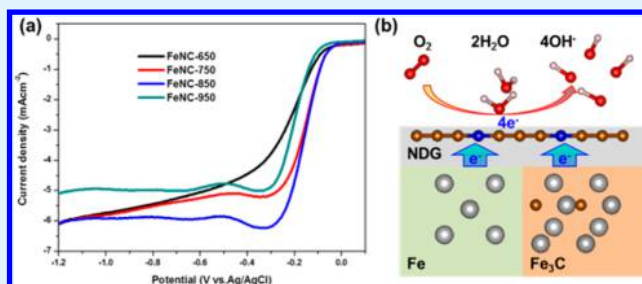
Jie Yang,[‡] Jiangtao Hu,[‡] Mouyi Weng,[‡] Rui Tan, Leilei Tian, Jinlong Yang, Joseph Amine, Jiaxin Zheng,* Haibiao Chen,* and Feng Pan*[✉]

School of Advanced Materials, Peking University, Shenzhen Graduate School, Shenzhen 518055, People's Republic of China

Supporting Information

ABSTRACT: Non-noble metal catalysts with catalytic activity toward oxygen reduction reaction (ORR) comparable or even superior to that of Pt/C are extremely important for the wide application of metal–air batteries and fuel cells. Here, we develop a simple and controllable strategy to synthesize Fe-cluster embedded in Fe₃C nanoparticles (designated as Fe₃C(Fe)) encased in nitrogen-doped graphitic layers (NDGLs) with graphitic shells as a novel hybrid nanostructure as an effective ORR catalyst by directly pyrolyzing a mixture of Prussian blue (PB) and glucose. The pyrolysis temperature was found to be the key parameter for obtaining a stable Fe₃C(Fe)@NDGL core–shell nanostructure with an optimized content of nitrogen. The optimized Fe₃C(Fe)@NDGL catalyst showed high catalytic performance of ORR comparable to that of the Pt/C (20 wt %) catalyst and better stability than that of the Pt/C catalyst in alkaline electrolyte. According to the experimental results and first principle calculation, the high activity of the Fe₃C(Fe)@NDGL catalyst can be ascribed to the synergistic effect of an adequate content of nitrogen doping in graphitic carbon shells and Fe-cluster pushing electrons to NDGL. A zinc–air battery utilizing the Fe₃C(Fe)@NDGL catalyst demonstrated a maximum power density of 186 mW cm⁻², which is slightly higher than that of a zinc–air battery utilizing the commercial Pt/C catalyst (167 mW cm⁻²), mostly because of the large surface area of the N-doped graphitic carbon shells. Theoretical calculation verified that O₂ molecules can spontaneously adsorb on both pristine and nitrogen doped graphene surfaces and then quickly diffuse to the catalytically active nitrogen sites. Our catalyst can potentially become a promising replacement for Pt catalysts in metal–air batteries and fuel cells.

KEYWORDS: Oxygen reduction reaction (ORR), N-doped graphitic layers, Fe₃C(Fe) cluster, Synergistic effect, Zn–air batteries



1. INTRODUCTION

Metal–air batteries and fuel cells have received great attention as next generation energy storage and conversion devices owing to the relatively high energy density, safety, and environmental benignity.^{1–5} As a cathode reaction in these devices, oxygen reduction reaction (ORR) is a crucial step affecting the overall performance. Due to the sluggish ORR kinetics,^{6–8} highly active and stable catalysts are extremely important. Traditional catalyst is based on noble metals, such as platinum supported on porous carbon. However, the high cost, limited resource, and unsatisfactory stability have seriously hampered the wide application of noble metal catalysts.^{9–12} Tremendous efforts have been put to developing nonprecious metal catalysts with comparable ORR performance at much lower cost. Examples include metal oxides,¹³ metal–N–C catalysts,^{14–16} and metal free catalysts.^{17,18}

Recently, Fe/Fe₃C encased in carbon shells has been reported as a novel type of highly active catalyst toward ORR, and many new methods have been adopted to prepare Fe/Fe₃C@C based catalyst.^{16,19–21} Meanwhile, the mechanism of ORR catalysis by Fe or Fe₃C encapsulated in carbon or nitrogen doped carbon

were investigated. Deng et al. synthesized Fe encapsulated in pristine and N-doped carbon nanotubes (CNTs) as an active ORR catalyst. They found that the encapsulated Fe can significantly enhance the ORR activity of CNTs. Density function theory (DFT) calculations showed that there is charge transfer from Fe to carbon which facilitates O₂ adsorption. Doping nitrogen into the graphitic layer can further reduce the local work function, leading to even better ORR performance.²² Li's group synthesized hollow spheres containing Fe₃C nanoparticles encapsulated in graphitic shells under high pressure as an ORR catalyst. It was noted that the catalytic activity of ORR drastically declined after the Fe₃C nanoparticles were removed by milling and subsequent acid leaching.¹⁹ More recently, a thorough study on Fe–N–C catalyst for ORR was reported by Wan's group. Their experimental and calculation results proved that both Fe/Fe₃C nanocrystals and Fe–N_x sites are essential to achieve high ORR performance.²³ Now it is mostly believed that

Received: October 16, 2016

Accepted: January 18, 2017

Published: January 18, 2017

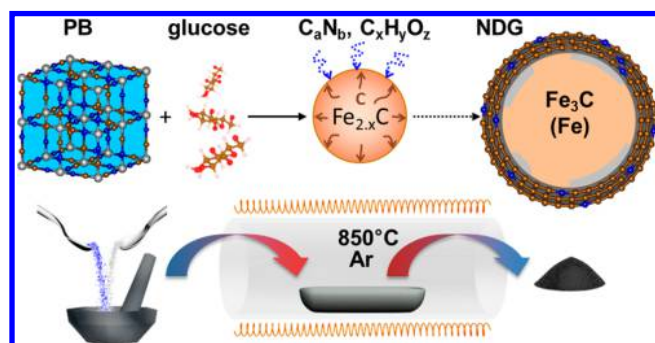
the active sites within a Fe/Fe₃C@C catalyst are situated in the outside surface of the graphitic shells which are activated by the encased Fe/Fe₃C cores inside. Although Fe/Fe₃C is not directly exposed to oxygen, the electronic effect between Fe/Fe₃C core and external carbon shells results in a decreased local work function on the surface of carbon shells, which facilitates O₂ adsorption. The synergistic effect of Fe/Fe₃C pushing electrons and nitrogen doping are the key factors for achieving superior ORR performance.

Many previously reported synthesis processes of Fe–N–C catalysts are relatively complicated and difficult to scale up. Herein, we report to synthesize Fe-cluster embedded in Fe₃C nanoparticles (designated as Fe₃C(Fe)) encased in nitrogen doped graphitic layers (NDGL) as a novel hybrid nanostructure (Fe₃C(Fe)@NDGL) as an effective ORR catalyst by directly pyrolyzing a mixture of Prussian blue (PB) and glucose. The synthesis could achieve to control the nitrogen doping content and embed Fe-clusters in Fe₃C. The catalyst showed very high catalytic activity of ORR comparable to the Pt/C (20 wt %) catalyst and better stability than the Pt/C catalyst in alkaline solution. The experimental results and DFT calculation indicated that the high activity of the optimized Fe₃C(Fe)@NDGL catalyst can be ascribed to the synergistic effect of Fe₃C(Fe) pushing electrons to nitrogen doped graphitic carbon shells and an adequate level of nitrogen doping. The precursor consists of only PB and glucose, which are both easily accessible and inexpensive. It takes only one pyrolysis to obtain the Fe₃C(Fe)@NDGL catalyst. Optimal Fe₃C(Fe)@NDGL core–shell nanostructure and nitrogen level can be achieved by controlling the pyrolysis temperature. The Fe₃C(Fe)@NDGL catalyst was evaluated by rotating disk electrode (RDE), which revealed excellent activity and durability in ORR under alkaline solution. Furthermore, the Fe₃C(Fe)@NDGL catalyst showed better performance than the Pt/C catalyst when tested in actual zinc–air batteries. A mechanism is proposed that the nitrogen doped graphitic carbon shells with a large surface area can spontaneously adsorb O₂ and quickly transfer O₂ to the catalytically active nitrogen sites by surface diffusion. The experimental results and theoretical calculations systematically explained why Fe₃C(Fe)@NDGL showed high ORR activity and even better performance in zinc–air batteries. Therefore, our catalyst is a potential and promising alternative to noble-metal catalysts applied in metal–air batteries and fuel cells.

2. EXPERIMENTAL SECTION

2.1. Catalyst Synthesis. The Fe₃C(Fe)@NDGL catalyst was synthesized according to a process schematically illustrated in Scheme 1.

Scheme 1. Synthesis of Fe₃C(Fe) Nanoparticles Encased in Nitrogen-Doped Graphitic Layers



During a synthesis process, commercial Prussian blue (0.5 g) and glucose (0.15 g) were mixed together with addition of distilled water and ethanol, and dispersed further by grinding in a mortar. And the mixture was slowly dried at 80 °C in an electric heat oven. Afterward, the powders were heated to a pyrolysis temperature in the range of 650–950 °C with 2 °C min⁻¹ and held at the pyrolysis temperatures for 6 h under an Argon atmosphere. To remove the unstable and catalytically inactive components, the pyrolyzed powders were leached in H₂SO₄ (0.5 M) solution at 80 °C for 12 h, followed by centrifugal collection and thorough water-washing. Eventually, the leached samples were dried at 80 °C in a vacuum oven. The yield of the catalyst was about 32%. The catalysts were denoted as FeNC-650, FeNC-750, FeNC-850, and FeNC-950, according to their pyrolysis temperatures of 650, 750, 850, and 950 °C, respectively.

2.2. Physical Characterization. The X-ray diffraction (XRD, Bruker D8-Advance diffractometer with Cu K α , $\lambda = 1.5405 \text{ \AA}$) was used to characterize the structure of the samples. Raman spectra were recorded by a Horiba modular Raman system (wavelength, $\lambda_0 = 532 \text{ nm}$). The scanning electron microscopy (SEM) was performed with a ZEISS Supra 55 field emission scanning electron microscopy. The images of transmission electron microscopy (TEM) were taken using an FEI TecnaiG2 F30. The X-ray photoelectron spectrometer (ESCALAB 250XL) was used to collect the X-ray photoelectron spectra (XPS). The specific surface area was determined by nitrogen adsorption/desorption method on a Micromeritics ASAP 2020 HD88. The pore size distributions were derived from the adsorption isotherm according to the Barrett–Joyner–Halenda (BJH) model.

2.3. Electrochemical Evaluation. All the electrochemical tests were performed in a three-electrode system using rotating disk electrode (RDE, Pine Instruments) with a glassy carbon electrode as the working electrode. The reference electrode and counter electrode are Ag/AgCl electrode and a Pt wire, respectively. The catalyst inks were prepared by ultrasonically dispersing the as-prepared catalyst (10 mg) in a 2 mL mixed solution for 30 min. The mixed solution was composed of 5 wt % Nafion (Dupont) and deionized water with volume ratio of 1:9. For comparison, 2 mg mL⁻¹ Pt/C (20 wt % Pt, Alpha Aesar) catalyst ink was prepared by following the same procedure. A 15 μL FeNC ink was pipetted on the glassy carbon electrode surface (5 mm diameter, 0.196 cm² geometric area) so that the catalyst loading is 0.38 mg cm⁻². The 20 wt % Pt/C loading was calculated to be 0.15 mg cm⁻², leading to Pt loading of 31 $\mu\text{g cm}^{-2}$. The electrolyte was 0.1 M aqueous KOH solution saturated with O₂.

The kinetic parameters of ORR can be analyzed by the Koutecky–Levich (KL) equation:

$$\frac{1}{J} = \frac{1}{J_K} + \frac{1}{J_L} = \frac{1}{J_K} + \frac{1}{Bw^{1/2}} \quad (1)$$

$$B = 0.2nFC_{\text{O}_2}D_{\text{O}_2}^{-1/3}\nu^{-1/6} \quad (2)$$

where J is the measured current density, J_K is the kinetic-limiting current density, and J_L is the diffusion-limiting current density, respectively; w is the rotation speed in rpm, n is the number of transferred electron per oxygen molecule, F is the Faraday constant ($F = 96485 \text{ C mol}^{-1}$), C_{O_2} is the bulk concentration of oxygen in the solution ($C_{\text{O}_2} = 1.2 \times 10^{-6} \text{ mol cm}^{-3}$), D_{O_2} is the diffusion coefficient of O₂ in 0.1 M KOH ($D_{\text{O}_2} = 1.9 \times 10^{-5} \text{ cm}^2 \text{ s}^{-1}$), and ν is the kinetic viscosity ($\nu = 0.01 \text{ cm}^2 \text{ s}^{-1}$).

According to the linear sweep voltammetry (LSV) curves, the corresponding kinetic current densities were derived by means of the following equation:

$$J_K = \frac{J_L}{J_L - J} \quad (3)$$

2.4. Zinc–Air Battery Test. The air electrodes were prepared by uniformly casting the catalyst ink on commercial Teflon-coated carbon fiber paper (SGL carbon paper, Germany). The catalyst ink was a mixture of 20 mg of the catalyst, 100 μL of 5 wt % Nafion solution, and 5 mL of ethanol. After ultrasonically dispersing for 1 h to form a homogeneous ink, the catalyst ink was uniformly casted on a 2.0 cm² carbon fiber paper, leading to a catalyst loading of 2.4 mg cm⁻².

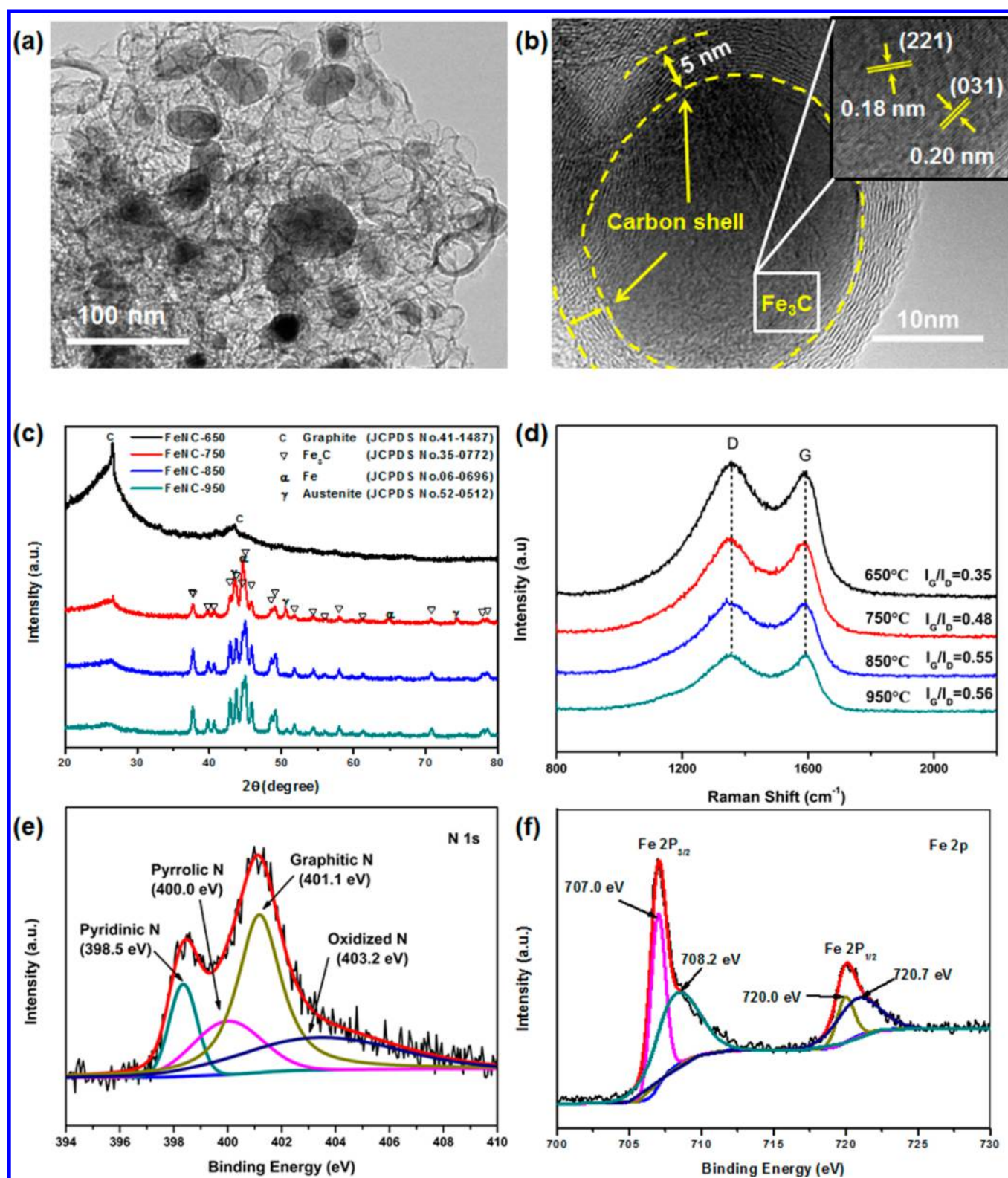


Figure 1. (a and b) TEM of FeNC-850. (c) XRD patterns. (d) Raman spectra. (e) High-resolution N 1s XPS of FeNC-850. (f) High-resolution Fe 2p XPS of FeNC-850.

Afterward, it was dried at 80 °C for 1 h. The battery was assembled using a zinc foil as the anode and 7 M KOH solution as the electrolyte. The battery was equipped with a pump to circulate the electrolyte during the test. The galvanostatic discharge test was carried out using a Neware Battery test instrument (Shenzhen Neware Instrument Company) at room temperature. To assess the cathode performance, the galvanody-

amic experiment was carried out using an electrochemical workstation (Princeton) at different current densities.

3. CALCULATION

First principle calculations were performed with generalized gradient approximation on projector augmented wave pseudo-

potential, which was implemented in the vienna ab initio simulation package (VASP). In order to match the lattice constant, the maximum change on the length of iron and Fe₃C was 7.38% and 5.40%, respectively. As the objective of the calculation was to study the trend of changes in graphene before and after adhering, we chose the most common low-index surface (001) both for Fe and Fe₃C. An energy cutoff of 450 eV and 4 × 6 × 1 Monkhorst–Pack was used in the graphene–iron system, and 3 × 2 × 1 Monkhorst–Pack was used in the graphene–Fe₃C system. A vacuum buffer space of 20 Å was set to eliminate the effect of the atoms from neighboring lattice both in the graphene–iron and graphene–Fe₃C system. During the geometry optimizations, we used six layers of Fe/Fe₃C atoms to simulate iron or Fe₃C beneath graphene. The bottom four layers of Fe/Fe₃C atoms are fixed to simulate the bulk iron or Fe₃C. We have also fixed the lattice constant. All calculations are spin-polarized. van der Waals interactions were also considered.

4. RESULTS AND DISCUSSION

When subjected to pyrolysis in an inert atmosphere, PB gradually decomposed to iron, carbon, nitrogen gas, various iron carbides (Fe₇C₃, Fe₂C, Fe₃C), and various carbon nitride gases (CN, C₂N₂⁺, C₃N₂⁺, C₃N₃⁺).^{14,24} Metallic iron or iron carbide nanoparticles catalyzed the deposition of nitrogen doped graphitic layers from the gaseous decomposition products of PB and glucose. The structure and the morphology of the samples were observed by SEM and TEM (Figure S1–S2). As shown in Figure S1c, the typical morphology of FeNC-850 is mainly spherical nanoparticle with a diameter about 30–40 nm. The detailed characteristics of the nanoparticles can be revealed by TEM (Figure 1a and b), which shows that the Fe₃C(Fe) nanoparticles are completely enclosed by graphitic layers with a thickness of about 5 nm, exhibiting a well-defined core–shell structure. Note that the interface layer between Fe₃C and graphitic layers should be the nitrogen doped graphene. During pyrolysis, Fe nanocrystals formed by the reduction of PB catalyzed the growth of nitrogen-doped graphitic layers on the surface of Fe, while parts of carbon dissolved in Fe formed Fe₃C crystalline during cooling, leading to the hybrid core–shell Fe₃C(Fe)@NDGL.^{25,26} The core–shell nanoparticles were further analyzed by high-resolution TEM (HRTEM). The image displays well-defined lattice fringes with space distance of 0.18 and 0.20 nm, which are consistent with the planes of (221) and (031) in the Fe₃C phase. Fe₃C(Fe) nanoparticles confined by graphitic layers are expected to improve the chemical activity of nitrogen doped graphitic layers where oxygen is activated and reduced.^{22,27}

Figure 1c shows the XRD patterns of catalysts synthesized at different temperatures followed by leaching in H₂SO₄. The two relatively wide peaks located at about 26.2° and 43.5° correspond to the (002) and (101) planes of the graphitic carbon,²⁸ and other peaks can be assigned to Fe₃C (JCPDS No. 35-0772), α-Fe (JCPDS No. 06-0696), and γ-Fe (JCPDS No. 52-0512).²⁰ The XRD data confirm the presence of graphitic carbon in all samples and Fe₃C in samples except FeNC-650. It also shows that there is a small amount of α-Fe and γ-Fe in FeNC-750, FeNC-850 and FeNC-950. Samples without H₂SO₄ leaching were also examined by XRD (Figure S3). Fe₂O₃ (JCPDS No. 39-1346) was identified in FeNC-650 before leaching, which was apparently removed by H₂SO₄ during leaching. Fe, Fe₂O₃, and Fe₃C were identified in FeNC-750 before leaching, and Fe₃C was identified in FeNC-850 and FeNC-950. Based on the XRD data, a possible mechanism is proposed. At 650 °C, metallic Fe and carbon

were formed when the precursor decomposed upon pyrolysis. At that temperature, growth of graphitic carbon catalyzed by Fe was sluggish and the carbon layers contained many pores/defects permeable to oxygen. Fe was oxidized to Fe₂O₃ when exposed to air, and then Fe₂O₃ was removed by H₂SO₄ during leaching. As the pyrolysis temperature increased, various iron carbides (Fe₇C₃, Fe₂C, and Fe₃C) started to form and less-defective graphitic carbon layers formed around the nanoparticles. Meanwhile, Fe₇C₃ and Fe₂C further transformed to Fe₃C with excess carbon segregating to the particle surface and reinforcing the carbon shells. The impermeable graphitic carbon shells protected Fe/Fe₃C from oxidation and H₂SO₄ leaching. Therefore, stable Fe₃C(Fe)@NDGL core–shell nanostructure cannot be obtained if the pyrolysis temperature is 650 °C or lower.

Raman spectra of the catalysts were collected to compare the degree of graphitization of the carbon shells (Figure 1d). D-band and G-band of the samples are located at ~1352 and ~1594 cm⁻¹, respectively.^{29–31} With the pyrolysis temperature increasing, the integral intensity ratio of I_G/I_D also follows an increasing trend (Figure S4). It suggests that a more ordered graphitic structure and less defects have been formed at a higher heat-treated temperature, which would improve the conductivity and thus promotes charge transfer. In addition, the graphitic carbon structure containing fewer pores/defects can offer better protection to the Fe₃C(Fe) cores. The Raman result further verified that pyrolysis temperature above 650 °C is essential to produce high-quality core/shell nanoparticles which can be stable in air and in acids.

Since the surface composition is of particular importance to catalytic performance, we further investigated the catalysts by XPS. The XPS survey reveals that the samples mainly consist of C, O, N, and Fe (Figure S5a). The atomic percentages of different elements are summarized in Table S1. As shown in Figure 1e, the high resolution N 1s spectrum could be assigned to four peaks which are pyridinic N (398.5 ± 0.2 eV), pyrrolic N (400 ± 0.2 eV), graphitic N (401 ± 0.2 eV), and oxidized N (403.0 ± 0.3 eV), respectively.^{32,33} Generally, pyridinic N and graphitic N are considered to be sp² hybridized, which would enhance the activity for ORR. Besides, pyridinic N and pyrrolic N are likely to form catalytically active Fe–N_x/C centers because of lone-pair electrons.^{34,35} And the contribution of oxidized N toward to ORR is unclear.³⁶ According to the integral area of corresponding peaks, the contents of different types of nitrogen were shown in Table 1. It is noted that the total nitrogen content

Table 1. Contents of Various Types of Nitrogen Sites Determined by XPS

catalyst	FeNC-650	FeNC-750	FeNC-850	FeNC-950
pyridinic N (at %)	4.14	1.71	0.60	0.20
pyrrolic N (at %)	2.70	1.73	0.65	0.35
graphitic N (at %)	2.33	1.76	1.43	0.96
oxidized N (at %)	1.64	1.45	1.06	0.87
total N (at %)	10.81	6.65	3.74	2.38

decreases with the temperatures increasing, which indicates that the unstable nitrogen sites tend to decompose at higher temperatures. By deconvolution, the high resolution Fe 2p_{3/2} spectrum (Figure 1f) can be assigned to metallic Fe (707.0 eV) and Fe in Fe₃C (708.2 eV), respectively, which is consistent with the observations by XRD. Due to the low signal intensity of Fe crystalline phase revealed by XRD, we infer that there are small

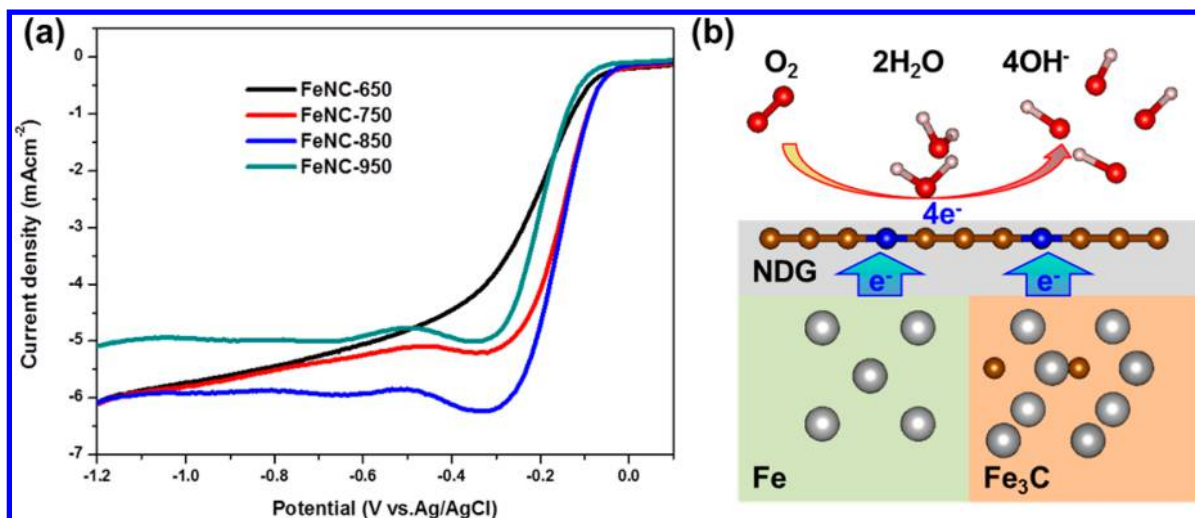


Figure 2. (a) Rotating disk electrode (RDE) voltammograms of all the samples in an O_2 -saturated 0.1 M KOH solution at a rotation speed of 1600 rpm with a scan rate of 10 mVs^{-1} . (b) Schematic representation of the ORR process at the surface of N-doped graphitic layers with Fe_3C encased.

domains containing zero-valence Fe atoms according to the XPS results.

The BET specific surface areas and pore sizes of the samples were derived from N_2 adsorption/desorption measurements (Figure S6). The specific surface areas were calculated to be 594, 573, 418, and $341 \text{ m}^2 \text{ g}^{-1}$ for FeNC-650, FeNC-750, FeNC-850, and FeNC-950, respectively. The specific surface area shows a downtrend with the pyrolysis temperature increasing, probably because of partial shrinkage of the carbon skeleton at higher temperatures. Generally, materials with a relatively high specific surface area would probably contain more catalytic sites and thus show high ORR performance. Utilizing the BJH model, the pore size distribution derived from the corresponding adsorption isotherm revealed pore diameters with a range from 10 to 100 nm, indicating that the samples mainly contain mesopores and macropores. It is believed that the mesopores and macropores facilitate the mass transfer of the ORR-related species such as O_2 , H_2O and OH^- , thus enhancing the ORR activity.^{37–39} Therefore, the $\text{Fe}_3\text{C}(\text{Fe})@\text{NDGL}$ catalyst with a relatively high surface area and adequate pore size distributions should be a good choice for ORR.

The catalytic activity of the catalysts was evaluated by RDE in alkaline solutions. As shown in Figure 2a, we first studied the ORR performance as a function of the pyrolysis temperature to preliminarily screen the catalyst with the highest activity in an O_2 -saturated 0.1 M KOH solution. According to the linear sweep voltammetry curves, the FeNC-850 exhibits the best ORR activity, which is judged by the onset potential, the half-wave potential and the diffusion-limiting current, shown in Table S2. In XRD and TEM analysis, we have observed that FeNC-750 and FeNC-950 catalysts show a microstructure similar to that of FeNC-850, while the FeNC-650 is mainly composed of carbon layers without Fe_3C core. It is noted that the onset potential and half-wave potential of FeNC-650 are both more negative than those of FeNC-750 and FeNC-850. It suggests that $\text{Fe}_3\text{C}(\text{Fe})$ core significantly enhances the catalytic activity even though it is not exposed to the solutions and O_2 . Although FeNC-650 has the largest specific surface area and highest nitrogen content, it does not show very high ORR activity. Previous works suggested that nitrogen doping is a precondition to form active sites in Fe-based or C-based ORR catalysts.^{40,41} So it can be inferred that the $\text{Fe}_3\text{C}(\text{Fe})$ nanoparticles have interacted with the graphitic

carbon shells to facilitate O_2 adsorption and reduction, as shown in Figure 2b. To some extent, the enhanced performance of FeNC-850 can be ascribed to the confinement effect of $\text{Fe}_3\text{C}(\text{Fe})$ encapsulated in the carbon shells, which is similar to the iron cluster within the CNT channels.⁴² Since the onset and half-wave potentials of FeNC-750 and FeNC-850 are almost equal, the main difference is the current density, which is likely ascribed to the different conductivity because the samples treated at the higher pyrolysis temperature ($850 \text{ }^\circ\text{C}$) can generate better electronic conductivity for graphitic carbon shells. When the temperature was further elevated to $950 \text{ }^\circ\text{C}$, the catalyst activity began to decrease, likely due to the reduced number of nitrogen sites. Obviously, the pyrolysis temperature directly affects the core–shell nanostructure (interaction between the $\text{Fe}_3\text{C}(\text{Fe})$ cores and the graphitic carbon shells), the electronic conductivity, the number of nitrogen sites, and the specific surface area. Therefore, this observation indicates that the outstanding ORR catalytic activity of FeNC-850 can be attributed to optimizing multiple factors.

Furthermore, we compared the ORR performance of the FeNC-850 catalyst and a Pt/C (20 wt %) catalyst, as shown in Figure 3a. In 0.1 M KOH, FeNC-850 displays relatively positive onset potential (-0.055 V vs Ag/AgCl) and half-wave potential (-0.152 V vs Ag/AgCl), respectively, which is comparable to those of the Pt/C catalyst (-0.041 and -0.134 V). To understand the reaction pathway for ORR, the kinetics of ORR was investigated by rotating disk electrode (RDE) from 225 to 2025 rpm and the kinetic parameters were calculated using the KL equation. It is noted that the diffusion-limiting current exhibits an increasing trend mainly because of the accelerated diffusion at higher speeds, shown in Figure 3b. The fitting KL plots exhibits very good linearity (Figure 3c), suggesting the first-order reaction kinetics toward the dissolved oxygen concentration and similar number of transferred electrons in ORR at various potentials.^{13,43,44} The number of transferred electrons was derived to be ~ 4 at various potentials from -0.30 to -0.70 V , indicating that a four-electron pathway dominated the ORR process.^{13,20,45} Additionally, based on the KL plots, the corresponding kinetic-limiting current density was calculated to be 33.09 mA cm^{-2} for FeNC-850 at the potential of -0.5 V (vs Ag/AgCl). It is nearly equal to the value of the Pt/C (33.26 mA cm^{-2}), as shown in Figure 3d. The corresponding Tafel slope

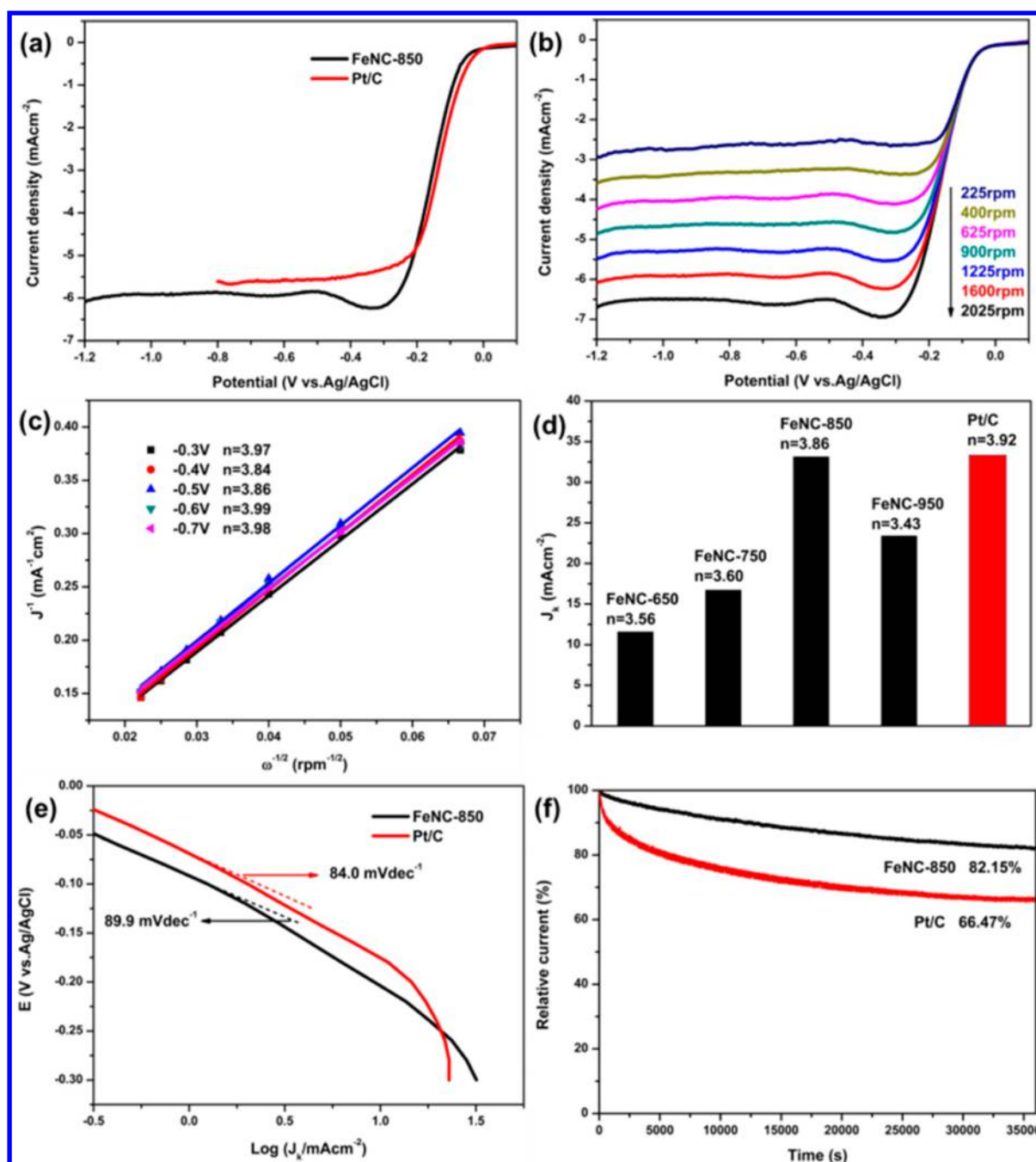


Figure 3. (a) LSV curves of FeNC-850 and Pt/C. (b) LSVs for FeNC-850 with various rotation rates. (c) Corresponding KL plots (j^{-1} vs $\omega^{-1/2}$) at different potentials. (d) Kinetic-limiting current densities and corresponding electron-transfer numbers at -0.50 . (e) Corresponding Tafel plots of FeNC-850 and Pt/C. (f) Chronoamperometric curves of FeNC-850 and Pt/C at -0.30 V in an O_2 -saturated 0.1 M KOH solution at 1600 rpm.

(Figure 3e) of FeNC-850 at low over potentials was calculated to be 89.9 mV dec^{-1} , which is close to that of the Pt/C (84.0 mV dec^{-1}), indicating that FeNC-850 has a good kinetic process similar to Pt/C catalyst. Since the durability of the catalyst is one of the major concerns in the practical application, the stability test of FeNC-850 and Pt/C were carried out at -0.3 V (vs Ag/AgCl) for 36000 s in an O_2 -saturated 0.1 M KOH solution at 1600 rpm, as shown in Figure 3f. It is noted that continuous oxygen reduction reaction based on the FeNC-850 catalyst electrode caused only a current loss of approximately 18% before stabilizing. By contrast, the current loss based on the 20 wt % Pt/C electrode was as high as about 34% under the same tested

conditions. Thus, the catalytic activity of FeNC-850 has a much better stability than that of the 20 wt % Pt/C in test situations.

It is well-known that the RDE (half-cell) test conditions are very different from the practical metal–air battery environment, where the electrolyte concentration is much higher and the diffusion coefficient as well as the solubility of oxygen is lower. It is quite necessary and important to evaluate the electrochemical performance of the catalyst in a practical metal–air battery. We first carried out a zinc–air battery test by discharging at a current density of 50 mA cm^{-2} , as shown in Figure 4b. The open circuit voltage of the zinc–air cell remained steady at 1.53 and 1.46 V for Pt/C and FeNC-850, respectively, which further confirmed that the intrinsic activity of FeNC-850 was close to that of Pt/C. After

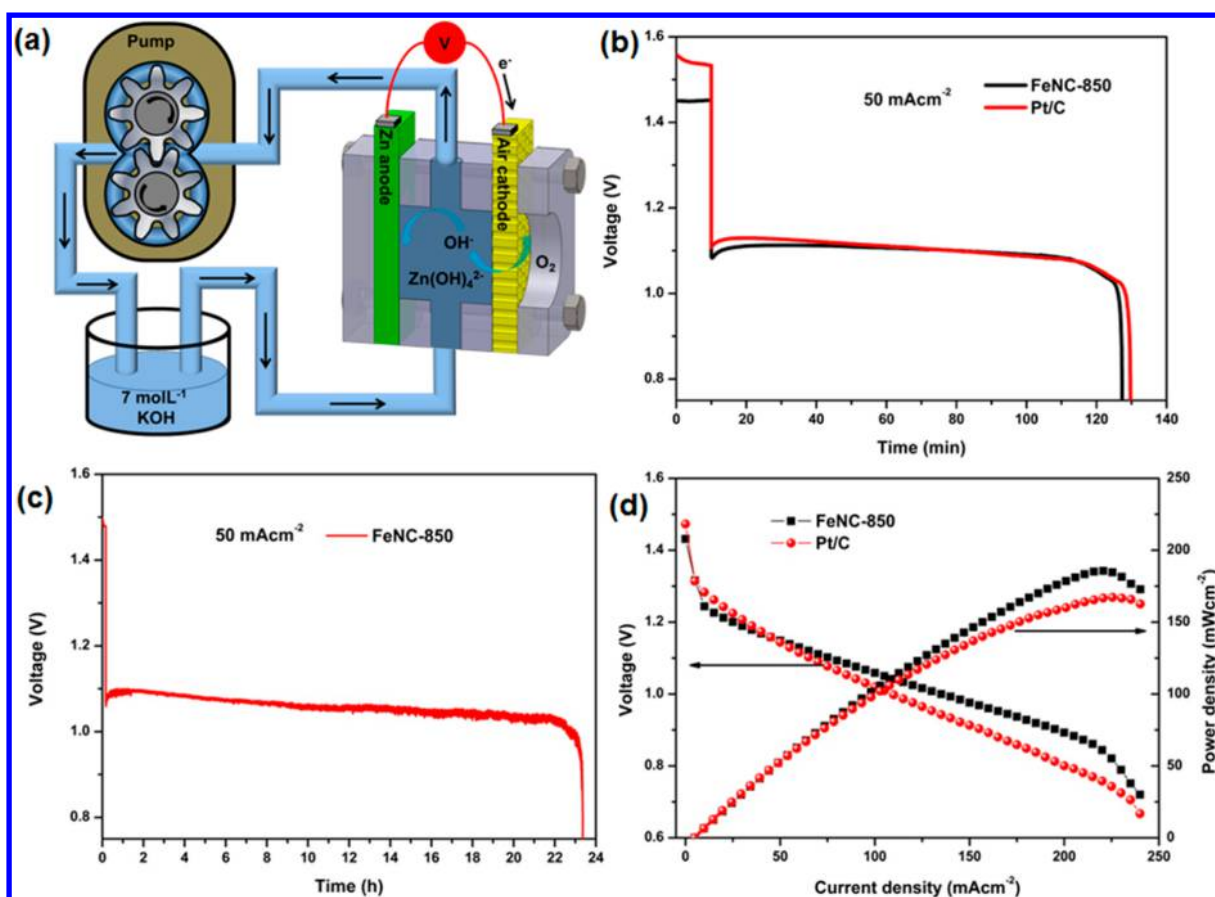


Figure 4. (a) Schematic of a Zn–air cell with pump-circulating electrolyte. (b) Discharge curves of Zn–air cells utilizing FeNC-850 and Pt/C catalysts in stagnant electrolyte. (c) Discharge curve of Zn–air cells with circulating electrolyte. (d) Current–voltage and current–power curves of Zn–air cells utilizing FeNC-850 and Pt/C catalysts.

discharging for approximately 2 h at the current density of 50 mA cm⁻², the voltage of the battery quickly dropped below 0.75 V. Based on the mass of consumed zinc, the actual specific capacities were both about 790 mAh g⁻¹ for zinc–air batteries using the FeNC-850 catalyst and the Pt/C catalyst (shown in Figure S8). When the zinc–air battery discharges, the zinc would be oxidized to form soluble Zn(OH)₄²⁻. When Zn(OH)₄²⁻ are supersaturated in the alkaline solution, they would decompose into insoluble ZnO.⁵ Once the zinc oxide deposits fully covered the surface of zinc electrode, the zinc anode was passivated and the discharge voltage quickly dropped before the zinc anode can be fully utilized. To prevent battery failure due to zinc oxide deposition, a new zinc–air device was equipped with a pump to circulate the electrolyte, shown in Figure 4a. Figure 4c depicts the discharge curve of zinc–air battery with electrolyte circulation at 50 mA cm⁻². Amazingly, the discharge time was extended to about 23 h until zinc was fully consumed. Replacing the spent zinc foil and the electrolyte without changing the air cathode could fully restore the performance the zinc–air battery, indicating excellent stability of the FeNC-850 catalyst. The current–voltage and current–power plots of zinc–air batteries are shown in Figure 4d. It is noted that there is a tiny gap in the discharge voltage and the output power between FeNC-850 and Pt/C catalysts at low current densities. But when it comes to higher current densities, a reverse trend has been observed. The voltage of the battery with Pt/C catalyst becomes lower than that of FeNC-850 catalyst. The corresponding peak power density of zinc–air battery based on FeNC-850 catalyst is about 186 mW

cm⁻², which is slightly higher than that of the zinc-battery with Pt/C catalyst (167 mW cm⁻²), indicating that the favorable pore structure of FeNC-850 catalyst can facilitate fast mass and charge transfer. Both results from the galvanodynamic test and galvanodischarge test showed that the electrochemical performance of the FeNC-850 catalyst was comparable or superior to that of the Pt/C (20 wt %) catalyst in the practical zinc–air battery. So FeNC-850 is a promising and potential catalyst toward ORR to be used in metal–zinc batteries and fuel cells.

Our first principle calculations show that there is a charge (electrons) transfer from Fe/Fe₃C to carbon layers from projected density of states (DOS) and bader charge analysis, indicating a positive effect on catalyzing for N-doped carbon layers when it is in contact with iron and Fe₃C, which can both be found beneath the carbon layers by XPS analysis. The transferred extra electrons are generally considered to be one of the key factors that enhance the ORR activity. We first calculated a series of systems with increasing iron atoms between N-doped graphene (NDG) and Fe₃C bulk. With the increasing number of iron atoms, the arrangement of iron atoms is shown to be Fe₃C-like configuration first and then Fe-metal-like configuration (Figure S9). This validates that Fe can exist between Fe₃C and carbon layers. For simplicity, we calculated the configuration of carbon layers on Fe and Fe₃C separately. We then considered one and two layers of carbon atoms above iron and Fe₃C surface separately. It can be found that the number of electrons on the surface carbon layer increases on both one layer and two layers system (Figure S10). Thus, we only calculated the case for one

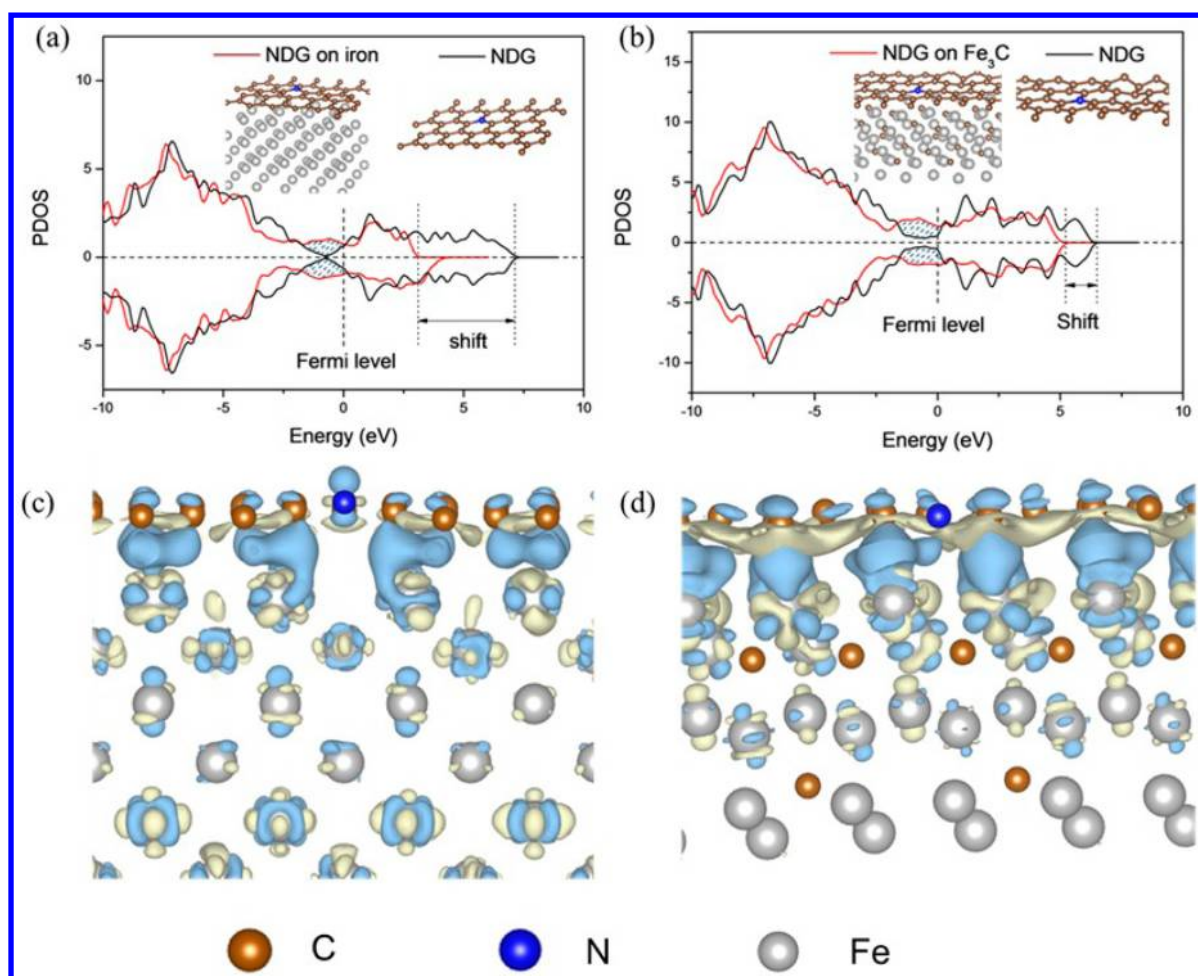


Figure 5. Projected density of states (DOS) on carbon layer in graphene-iron system (a) and graphene- Fe_3C system (b). The black and red lines in each graph represent the DOS of nitrogen doped graphene (NDG) before and after contacted with Fe or Fe_3C . The shadow areas in parts a and b illustrate the extra electrons transferred from Fe/ Fe_3C to NDG layer. The charge difference densities for NDG/Fe system and NDG/ Fe_3C system before and after contacting are plotted in parts c and d, respectively. The light blue areas indicate the areas gaining electrons, and the light yellow areas indicate the areas losing electrons. The same isosurface level of the boundary for both systems is adopted.

layer of N-doped graphene on Fe and Fe_3C . The geometric matching was implemented separately on graphene-iron and graphene- Fe_3C systems. As a result, the proportions of doped nitrogen atoms were different for the two systems, 2.5% and 1.6% in graphene-iron and graphene- Fe_3C , respectively. In order to eliminate the influence caused by different nitrogen proportion, we only compared the differences between NDG-iron (NDG- Fe_3C) system and NDG in the same lattice structure.

In project DOS analysis (Figure 5a and b), it can be observed that there is a significant leftward shift after NDG adhering on iron and Fe_3C . The leftward movement demonstrates the upward shift of Fermi level and the increasing of electrons on NDG. The shadow area also provides evidence that NDG layer gains electrons from Fe or Fe_3C . Moreover, it can also be seen that compared with Fe_3C , the upward shift of the Fermi level in NDG-Fe system is much more significant, indicating more charge transfer from Fe to NDG layers and a much better activity for ORR in NDG-Fe system. The bader charge analysis illustrates the same trend. The NDG layer gains 0.055 electrons per atom from Fe and 0.051 electrons per atom from Fe_3C for the NDG- Fe_3C system. Considering lower nitrogen content in graphene layer on Fe_3C , which should be more capable to gain electrons from Fe or Fe_3C , it can be concluded that iron can provide more electrons to carbon layers than that of Fe_3C . From

the charge difference density analysis (Figure 5c and d), we can see that more extra-electrons are transferred to NDG layer in NDG-iron system (especially for the nitrogen atom), indicating a more significant improvement on catalytic activity by iron than by Fe_3C .

Additionally, DFT calculation was performed to explain why $\text{Fe}_3\text{C}(\text{Fe})@\text{NDGL}$ catalyst achieved higher peak power density than commercial Pt/C catalyst in Zn-air batteries. The calculation of adsorption energy suggested that O_2 can spontaneously adsorb onto pristine and nitrogen doped graphene surface (Figure S11 and Table S4). Also, calculation showed that the diffusion on the surface of graphene is 3 orders of magnitude faster than that in the electrolyte solution (Figure S11). Therefore, the whole surface of the NDG layer in contact with the electrolyte solution can effectively capture O_2 molecules, which would quickly diffuse to the active sites on the continuous graphene surface. For Pt/C catalyst, O_2 molecules can only adsorb onto scattered Pt clusters and react. Combined with a large surface area of the N-doped graphitic matrix, the $\text{Fe}_3\text{C}(\text{Fe})@\text{NDGL}$ catalyst will definitely have a larger catalytically active surface area, leading to higher current density and power density.

5. CONCLUSIONS

In summary, we have developed a new synthesis method for producing $\text{Fe}_3\text{C}(\text{Fe})@\text{NDGL}$ with a core-shell structure by simply pyrolyzing a mixture of commercial PB and glucose under ambient pressure. Since the nitrogen content and the core-shell structure of the as-prepared materials can be controllably tuned by the pyrolysis temperature, we were able to optimize the synergetic effect between the $\text{Fe}_3\text{C}(\text{Fe})$ nanoparticle and the N-doped graphitic carbon shells for achieving superior catalytic performance. The catalyst exhibited excellent ORR performance comparable to the Pt/C catalyst and better stability than the Pt/C catalyst in alkaline medium by RDE tests. According to first principle calculation and experimental results, the high catalytic performance of the optimized FeNC-850 can be ascribed to the synergetic effect of $\text{Fe}_3\text{C}(\text{Fe})$ pushing electrons to NDGL and adequate nitrogen doping. Note that the Fe metal-domain sandwiched between NDGL and Fe_3C layers can provide more electrons to NDGL than Fe_3C , by which more extra-electrons are transferred to the N-sites in NDG-iron system to enhance ORR. The high performance of the catalyst was further demonstrated in zinc-air batteries. The battery based on FeNC-850 air cathode showed a maximum power density of 186 mW cm^{-2} , exceeding that with Pt/C catalyst (167 mW cm^{-2}), in which the unique mesopores and macropores of $\text{Fe}_3\text{C}(\text{Fe})@\text{NDGL}$ can facilitate O_2 transferring to active centers for catalysis and enhance the performance of ORR kinetics. Considering that the synthesis method utilizes inexpensive precursor and does not require organic solvents, templates, or high pressures, it is very suitable for large-scale production and wide application in metal-air batteries.

■ ASSOCIATED CONTENT

Supporting Information

The Supporting Information is available free of charge on the ACS Publications website at DOI: 10.1021/acsami.6b13166.

Additional characterization results including SEM, TEM, XRD, Raman, XPS, and additional details about electrochemical measurements and DFT calculations (PDF)

■ AUTHOR INFORMATION

Corresponding Authors

*E-mail: zhengjx@pkusz.edu.cn (J.Z.).

*E-mail: chenhb@pkusz.edu.cn (H.C.).

*E-mail: panfeng@pkusz.edu.cn (F.P.).

ORCID

Feng Pan: 0000-0002-8216-1339

Author Contributions

‡J.Y., J.H., and M.W.: These authors contributed equally.

Notes

The authors declare no competing financial interest.

■ ACKNOWLEDGMENTS

The research was financially supported by Guangdong Innovation Team Project (No. 2013N080), Shenzhen Peacock Plan (Grant KYPT20141016105435850), and Shenzhen Science and Technology Research Grant (nos. ZDSY20130331145131323, JCYJ20140903101633318, JCYJ20140903101617271, and JCYJ20140509093817681).

■ REFERENCES

- (1) Lee, J.-S.; Kim, S. T.; Cao, R.; Choi, N.-S.; Liu, M.; Lee, K. T.; Cho, J. Metal-Air Batteries with High Energy Density: Li-Air versus Zn-Air. *Adv. Energy Mater.* **2011**, *1*, 34–50.
- (2) Li, Y.; Gong, M.; Liang, Y.; Feng, J.; Kim, J.-E.; Wang, H.; Hong, G.; Zhang, B.; Dai, H. Advanced Zinc-Air Batteries Based on High-Performance Hybrid Electrocatalysts. *Nat. Commun.* **2013**, *4*, 1805–1813.
- (3) Nam, G.; Park, J.; Kim, S. T.; Shin, D.-b.; Park, N.; Kim, Y.; Lee, J.-S.; Cho, J. Metal-Free Ketjenblack Incorporated Nitrogen-Doped Carbon Sheets Derived from Gelatin as Oxygen Reduction Catalysts. *Nano Lett.* **2014**, *14*, 1870–1876.
- (4) Sapkota, P.; Kim, H. Zinc-Air Fuel Cell, a Potential Candidate for Alternative Energy. *J. Ind. Eng. Chem.* **2009**, *15*, 445–450.
- (5) Li, Y.; Dai, H. Recent Advances in Zinc-Air Batteries. *Chem. Soc. Rev.* **2014**, *43*, 5257–5275.
- (6) Chen, S.; Bi, J.; Zhao, Y.; Yang, L.; Zhang, C.; Ma, Y.; Wu, Q.; Wang, X.; Hu, Z. Nitrogen-Doped Carbon Nanocages as Efficient Metal-Free Electrocatalysts for Oxygen Reduction Reaction. *Adv. Mater.* **2012**, *24*, 5593–5597.
- (7) Steele, B. C. H.; Heinzel, A. Materials for Fuel-Cell Technologies. *Nature* **2001**, *414*, 345–352.
- (8) Xiong, W.; Du, F.; Liu, Y.; Perez, A., Jr.; Supp, M.; Ramakrishnan, T. S.; Dai, L.; Jiang, L. 3-D Carbon Nanotube Structures Used as High Performance Catalyst for Oxygen Reduction Reaction. *J. Am. Chem. Soc.* **2010**, *132*, 15839–15841.
- (9) Liang, J.; Zhou, R. F.; Chen, X. M.; Tang, Y. H.; Qiao, S. Z. Fe-N Decorated Hybrids of CNTs Grown on Hierarchically Porous Carbon for High-Performance Oxygen Reduction. *Adv. Mater.* **2014**, *26*, 6074–6079.
- (10) Bashyam, R.; Zelenay, P. A Class of Non-Precious Metal Composite Catalysts for Fuel Cells. *Nature* **2006**, *443*, 63–66.
- (11) Gong, K.; Du, F.; Xia, Z.; Durstock, M.; Dai, L. Nitrogen-Doped Carbon Nanotube Arrays with High Electrocatalytic Activity for Oxygen Reduction. *Science* **2009**, *323*, 760–764.
- (12) Li, Y.; Zhou, W.; Wang, H.; Xie, L.; Liang, Y.; Wei, F.; Idrobo, J.-C.; Pennycook, S. J.; Dai, H. An Oxygen Reduction Electrocatalyst Based on Carbon Nanotube-Graphene Complexes. *Nat. Nanotechnol.* **2012**, *7*, 394–400.
- (13) Liang, Y.; Li, Y.; Wang, H.; Zhou, J.; Wang, J.; Regier, T.; Dai, H. Co_3O_4 Nanocrystals on Graphene as a Synergistic Catalyst for Oxygen Reduction Reaction. *Nat. Mater.* **2011**, *10*, 780–786.
- (14) Wen, Z.; Ci, S.; Zhang, F.; Feng, X.; Cui, S.; Mao, S.; Luo, S.; He, Z.; Chen, J. Nitrogen-Enriched Core-Shell Structured Fe/ Fe_3C -C Nanorods as Advanced Electrocatalysts for Oxygen Reduction Reaction. *Adv. Mater.* **2012**, *24*, 1399–1404.
- (15) Proietti, E.; Jaouen, F.; Lefèvre, M.; Larouche, N.; Tian, J.; Herranz, J.; Dodelet, J. P. Iron-Based Cathode Catalyst with Enhanced Power Density in Polymer Electrolyte Membrane Fuel Cells. *Nat. Commun.* **2011**, *2*, 416.
- (16) Xiao, M.; Zhu, J.; Feng, L.; Liu, C.; Xing, W. Meso/Macroporous Nitrogen-Doped Carbon Architectures with Iron Carbide Encapsulated in Graphitic Layers as an Efficient and Robust Catalyst for the Oxygen Reduction Reaction in Both Acidic and Alkaline Solutions. *Adv. Mater.* **2015**, *27*, 2521–2527.
- (17) Hu, Y. S.; Adelhelm, P.; Smarsly, B.; Hore, S.; Antonietti, M.; Maier, J. Synthesis of Hierarchically Porous Carbon Monoliths with Highly Ordered Microstructure and Their Application in Rechargeable Lithium Batteries with High-Rate Capability. *Adv. Funct. Mater.* **2007**, *17*, 1873–1878.
- (18) Zhou, M.; Wang, H. L.; Guo, S. Towards High-efficiency Nanoelectrocatalysts for Oxygen Reduction through Engineering Advanced Carbon Nanomaterials. *Chem. Soc. Rev.* **2016**, *45*, 1273–1307.
- (19) Hu, Y.; Jensen, J. O.; Zhang, W.; Cleemann, L. N.; Xing, W.; Bjerrum, N. J.; Li, Q. Hollow Spheres of Iron Carbide Nanoparticles Encased in Graphitic Layers as Oxygen Reduction Catalysts. *Angew. Chem., Int. Ed.* **2014**, *53*, 3675–3679.
- (20) Yang, W.; Liu, X.; Yue, X.; Jia, J.; Guo, S. Bamboo-Like Carbon Nanotube/ Fe_3C Nanoparticle Hybrids and Their Highly Efficient

Catalysis for Oxygen Reduction. *J. Am. Chem. Soc.* **2015**, *137*, 1436–1439.

(21) Fan, X.; Peng, Z.; Ye, R.; Zhou, H.; Guo, X. M_3C (M: Fe, Co, Ni) Nanocrystals Encased in Graphene Nanoribbons: an Active and Stable Bifunctional Electrocatalyst for Oxygen Reduction and Hydrogen Evolution Reactions. *ACS Nano* **2015**, *9*, 7407–7418.

(22) Deng, D.; Yu, L.; Chen, X.; Wang, G.; Jin, L.; Pan, X.; Deng, J.; Sun, G.; Bao, X. Iron Encapsulated within Pod-Like Carbon Nanotubes for Oxygen Reduction Reaction. *Angew. Chem., Int. Ed.* **2013**, *52*, 371–375.

(23) Jiang, W.-J.; Gu, L.; Li, L.; Zhang, Y.; Zhang, X.; Zhang, L.-J.; Wang, J.-Q.; Hu, J.-S.; Wei, Z.; Wan, L.-J. Understanding the High Activity of Fe-N-C Electrocatalysts in Oxygen Reduction: Fe/Fe₃C Nanoparticles Boost the Activity of Fe-Nx. *J. Am. Chem. Soc.* **2016**, *138*, 3570–3578.

(24) Aparicio, C.; Machala, L.; Marusak, Z. Thermal Decomposition of Prussian Blue under Inert Atmosphere. *J. Therm. Anal. Calorim.* **2012**, *110*, 661–669.

(25) Hu, J.; Zheng, J.; Tian, L.; Duan, Y.; Lin, L.; Cui, S.; Peng, H.; Liu, T.; Guo, H.; Wang, X.; Pan, F. A Core-shell Nanohollow- γ -Fe₂O₃@Graphene Hybrid Prepared through the Kirkendall Process as a High Performance Anode Material for Lithium Ion Batteries. *Chem. Commun.* **2015**, *51*, 7855–7858.

(26) Hu, J.; Li, W.; Liu, C.; Tang, H.; Liu, T.; Guo, H.; Song, X.; Zheng, J.; Liu, Y.; Duan, Y.; Pan, F. The Formation and Mechanism of Nano-Monocrystalline γ -Fe₂O₃ with Graphene-Shell for High-Performance Lithium Ion Batteries. *RSC Adv.* **2016**, *6*, 51777–51782.

(27) Wen, Z.; Ci, S.; Zhang, F.; Feng, X.; Cui, S.; Mao, S.; Luo, S.; He, Z.; Chen, J. Nitrogen-Enriched Core-Shell Structured Fe/Fe₃C-C Nanorods as Advanced Electrocatalysts for Oxygen Reduction Reaction. *Adv. Mater.* **2012**, *24*, 1399–1404.

(28) Liu, R.; Wu, D.; Feng, X.; Mullen, K. Nitrogen-Doped Ordered Mesoporous Graphitic Arrays with High Electrocatalytic Activity for Oxygen Reduction. *Angew. Chem., Int. Ed.* **2010**, *49*, 2565–2569.

(29) Li, J. S.; Li, S. L.; Tang, Y. J.; Han, M.; Dai, Z. H.; Bao, J. C.; Lan, Y. Q. Nitrogen-Doped Fe/Fe₃C@Graphitic Layer/Carbon Nanotube Hybrids Derived from MOFs: Efficient Bifunctional Electrocatalysts for ORR and OER. *Chem. Commun.* **2015**, *51*, 2710–2713.

(30) Shao, Y. Y.; Zhang, S.; Engelhard, M. H.; Li, G. S.; Shao, G. C.; Wang, Y.; Liu, J.; Aksay, I. A.; Lin, Y. H. Nitrogen-Doped Graphene and Its Electrochemical Applications. *J. Mater. Chem.* **2010**, *20*, 7491–7496.

(31) Qu, L. T.; Liu, Y.; Baek, J. B.; Dai, L. M. Nitrogen-Doped Graphene as Efficient Metal-Free Electrocatalyst for Oxygen Reduction in Fuel Cells. *ACS Nano* **2010**, *4*, 1321–1326.

(32) Wang, H.; Maiyalagan, T.; Wang, X. Review on Recent Progress in Nitrogen-Doped Graphene: Synthesis, Characterization, and Its Potential Applications. *ACS Catal.* **2012**, *2*, 781–794.

(33) Sheng, Z.-H.; Shao, L.; Chen, J.-J.; Bao, W.-J.; Wang, F.-B.; Xia, X.-H. Catalyst-Free Synthesis of Nitrogen-Doped Graphene via Thermal Annealing Graphite Oxide with Melamine and Its Excellent Electrocatalysis. *ACS Nano* **2011**, *5*, 4350–4358.

(34) Lin, L.; Zhu, Q.; Xu, A.-W. Noble-Metal-Free Fe-N/C Catalyst for Highly Efficient Oxygen Reduction Reaction under Both Alkaline and Acidic Conditions. *J. Am. Chem. Soc.* **2014**, *136*, 11027–11033.

(35) Niu, W.; Li, L.; Liu, X.; Wang, N.; Liu, J.; Zhou, W.; Tang, Z.; Chen, S. Mesoporous N-Doped Carbons Prepared with Thermally Removable Nanoparticle Templates: an Efficient Electrocatalyst for Oxygen Reduction Reaction. *J. Am. Chem. Soc.* **2015**, *137*, 5555–5562.

(36) Hou, Y.; Huang, T.; Wen, Z.; Mao, S.; Cui, S.; Chen, J. Metal-Organic Framework-Derived Nitrogen-Doped Core-Shell-Structured Porous Fe/Fe₃C@C Nanoboxes Supported on Graphene Sheets for Efficient Oxygen Reduction Reactions. *Adv. Energy Mater.* **2014**, *4*, 1400337.

(37) Liang, H.-W.; Zhuang, X.; Bruller, S.; Feng, X.; Mullen, K. Hierarchically Porous Carbons with Optimized Nitrogen Doping as Highly Active Electrocatalysts for Oxygen Reduction. *Nat. Commun.* **2014**, *5*, 4973–4979.

(38) Wei, W.; Liang, H.; Parvez, K.; Zhuang, X.; Feng, X.; Mullen, K. Nitrogen-Doped Carbon Nanosheets with Size-Defined Mesopores as

Highly Efficient Metal-Free Catalyst for the Oxygen Reduction Reaction. *Angew. Chem., Int. Ed.* **2014**, *53*, 1570–1574.

(39) Liang, J.; Zheng, Y.; Chen, J.; Liu, J.; Hulicova-Jurcakova, D.; Jaroniec, M.; Qiao, S. Z. Facile Oxygen Reduction on a Three-Dimensionally Ordered Macroporous Graphitic C₃N₄/Carbon Composite Electrocatalyst. *Angew. Chem., Int. Ed.* **2012**, *51*, 3892–3896.

(40) Jaouen, F.; Proietti, E.; Lefevre, M.; Chenitz, R.; Dodelet, J.-P.; Wu, G.; Chung, H. T.; Johnston, C. M.; Zelenay, P. Recent Advances in Non-precious Metal Catalysis for Oxygen Reduction Reaction in Polymer Electrolyte Fuel Cells. *Energy Environ. Sci.* **2011**, *4*, 114–130.

(41) Lalonde, G.; Cote, R.; Guay, D.; Dodelet, J. P.; Weng, L. T.; Bertrand, P. Is Nitrogen Important in the Formulation of Fe-based Catalysts for Oxygen Reduction in Solid Polymer Fuel Cells? *Electrochim. Acta* **1997**, *42*, 1379–1388.

(42) Chen, W.; Fan, Z.; Pan, X.; Bao, X. Effect of Confinement in Carbon Nanotubes on the Activity of Fischer–Tropsch Iron Catalyst. *J. Am. Chem. Soc.* **2008**, *130*, 9414–9419.

(43) Mayrhofer, K. J. J.; Strmcnik, D.; Blizanac, B. B.; Stamenkovic, V.; Arenz, M.; Markovic, N. M. Measurement of Oxygen Reduction Activities via the Rotating Disc Electrode Method: From Pt Model Surfaces to Carbon-Supported High Surface Area Catalysts. *Electrochim. Acta* **2008**, *53*, 3181–3188.

(44) Wu, Z.; Xu, X.; Hu, B.; Liang, H.; Lin, Y.; Chen, L.; Yu, S. Iron Carbide Nanoparticles Encapsulated in Mesoporous Fe-N-Doped Carbon Nanofibers for Efficient Electrocatalysis. *Angew. Chem., Int. Ed.* **2015**, *54*, 8179–8183.

(45) Xia, W.; Mahmood, A.; Liang, Z.; Zou, R.; Guo, S. Earth-Abundant Nanomaterials for Oxygen Reduction. *Angew. Chem., Int. Ed.* **2016**, *55*, 2650–2676.